Carbon 190 (2022) 276–290

Contents lists available at ScienceDirect

Carbon

journal homepage: www.elsevier.com/locate/carbon

Atomic-scale probing of defect-assisted Ga intercalation through graphene using ReaxFF molecular dynamics simulations

Nadire Nayir [a, b, c], Mert Y. Sengul [d, e], Anna L. Costine [f], Petra Reinke [f], Siavash Rajabpour [g], Anushka Bansal [e], Azimkhan Kozhakhmetov [e], Joshua Robinson [a, e], Joan M. Redwing [a, e], Adri van Duin [a, c, *]

[a] 2D Crystal Consortium Material Innovation Platform (2DCC-MPI) Materials Research Institute, The Pennsylvania State University, University Park, PA, 16802, United States
[b] Department of Physics, Karamanoglu Mehmetbey University, Karaman, 70000, Turkey
[c] Department of Mechanical Engineering, The Pennsylvania State University, University Park, PA, 16802, United States
[d] Department of Pharmaceutical Sciences, University of Maryland, Baltimore, MD, United States
[e] Department of Materials Science and Engineering, The Pennsylvania State University, University Park, PA, 16802, United States
[f] Department of Materials Science and Engineering, University of Virginia, Charlottesville, VA, 22904, United States
[g] Department of Chemical Engineering, The Pennsylvania State University, University Park, PA, 16802, United States

ARTICLE INFO

Article history:
Received 10 November 2021
Received in revised form
21 December 2021
Accepted 4 January 2022
Available online 6 January 2022

ABSTRACT

We report a joint theory and experimental investigation on the defect-mediated surface interactions of gallium (Ga) metals and trimethyl-gallium (TMGa) molecules with graphene. A combination of Raman spectra, X-ray photoelectron spectroscopy, scanning tunneling microscopy and spectroscopy (STM/STS) reveal defects in graphene, which can act as pathways for Ga intercalation. These experimental results are connected to ReaxFF simulations, which further confirm that the Ga and TMGa adsorption on graphene is strongly impacted by the presence and size of defects. These defects catalyze the surface reactions by lowering the temperature for Ga-deposition on the surface. Moreover, multivacancy defects promote Ga intercalation through graphene by reducing the kinetic barrier while the migration through single vacancy or 5-8-5 defect is kinetically hindered. The ReaxFF results indicate that TMGa exposure leads to defect healing by the passivation of carbon-dangling bonds by hydrocarbon and organometallic adducts, which is supported by the decreased Raman D:G ratio in Ga-intercalated graphene and by STM images. Since probing and controlling graphene defects constitutes a key step in the intercalation mechanism, this work provides an in-depth atomic scale understanding into the complex interplay between defects and precursors, thus providing an effective way to design defects for 2D metal fabrication.

1. Introduction

Atomically thin two-dimensional (2D) materials with non-layered structure have gained widespread attention due to their exceptional electrical transport, optical, catalytic and thermal properties [1–4]. However, contrary to van der Waals layered 2D structures such as transition metal dichalcogenides [5–10], h-BN [11,12] and graphene [13,14], the synthesis of 2D nonlayered materials through direct epitaxy remains challenging as lattice mismatch typically drives a 3D growth mode. The exfoliation of

Abbreviations: MV, Monovacancy; DV, Divacancy; 3V, Trivacancy; 4V, Tetravacancy; 5V, Pentavacancy; 6V, Hexavacancy; 7V, Heptavacancy; 8V, Octavacancy; 16V, Sixteenvacancy; TMGa, Trimethylgallium; DMGa, Dimethylgallium; MMGa, Monomethylgallium; DFT, Density Functional theory; NEB, Nudge elastic band; MD, Molecular dynamics; STM and STS, Scanning tunneling microscopy and spectroscopy; XPS, X-ray photoelectron spectroscopy; EG, Epitaxial graphene; MOCVD, Metal organic chemical vapor deposition; CVD, Chemical vapor deposition; CV, Collective variable.

* Corresponding author. 2D Crystal Consortium Material Innovation Platform (2DCC-MPI) Materials Research Institute, The Pennsylvania State University, University Park, PA, 16802, United States.
E-mail address: acv13@psu.edu (A. van Duin).

https://doi.org/10.1016/j.carbon.2022.01.005
0008-6223/

ultra-thin layers from their respective non-layered bulk form is also difficult due to the strong chemical interlayer bonding [15,16]. Intercalation techniques have been identified as an alternative and novel technique [1,2,17–20] that enables to confine and stabilize nonlayered materials in their 2D form at the interface of a cap layer and substrate without sacrificing the quality of grown crystal. Recent studies [1,2,19,20] also show that epitaxial graphene (EG) on SiC serves as an ideal platform for the confinement heteroepitaxy of 2D metals and their compounds. At such a heterointerface, intercalants interact with epitaxial graphene through weak van der Waals forces while exhibiting covalent bonding to the SiC surface [1,2,21].

Defect engineering strategies have been regarded as an effective approach to tailor the physiochemical properties of graphene. Local manipulation of a graphene lattice by methods such as plasma treatment [1,21,22] and ion or electron beam bombardment [23] are used to generate defects, thereby enhancing the catalytic performance of the surface. In particular, Briggs et al. [1] demonstrated that the plasma-treatment (He and O_2) of EG before the intercalation modifies the EG transport properties, thus facilitating the migration of metals through graphene at the EG/SiC interface. However, the complex interplay between EG defects and metal intercalation in a chemical vapor deposition environment is not yet fully understood. In additional, the atomistic reaction pathways leading to the CVD/metal organic chemical vapor deposition (MOCVD) growth of a 2D layer cannot readily be obtained via experimental measurements. This has motivated the development of multiscale modeling that can substantially improve the atomic-scale understanding, and thus enhance the ability to control the intercalation mechanism during the growth. To date, first principles methods have been employed extensively to investigate the reaction kinetics of metal/surface interactions with bare and functionalized graphene [1,24]. However, to the best of our knowledge, no empirical potential exists to describe the surface reactions of Ga metal and trimethyl Ga (TMGa) with graphene with/without defects but is sorely needed – given the need for large (>1000 atoms) long-time (>1 ns) dynamics simulations associated with 2D MOCVD growth. Recently Rajapbour et al. [25] reported a ReaxFF reactive force field developed particularly for the MOCVD gas-phase reactions during the 2D Ga/In growth that enables us to provide this large-scale, long-time atomistic scale perspective.

In this study, the ReaxFF reactive force field developed by Rajabpour et al. [25] was extended to the surface reactions in the CVD/MOCVD growth of 2D-Ga metal on graphene. Then, combining experimental measurements with atomistic-scale simulations, the complex interplay between the EG defects and Ga intercalation was investigated. To this end, molecular dynamics (MD) and meta dynamics simulations were employed to illuminate the impact of precursor, temperature, defect size and density on the Ga binding and penetration to/through graphene. Scanning tunneling microscopy (STM) and spectroscopy (STS) along with Raman spectra and X-ray photoelectron spectroscopy (XPS) were further deployed to identify defects on EG before and after the Ga intercalation in the MOCVD environment. The details of the force field parameter fitting process, training results and optimized force field parameters can be found in the Methods section and supporting information.

2. Methods

2.1. Theoretical method

ReaxFF Reactive Force Field: The ReaxFF reactive force field [26] is an interatomic potential that describes chemical events and electrostatic interactions through the combination of the bond order formalism with polarizable charge description. The distance-dependent bond order indicates the bond stability between atom pairs and updated at each MD iteration, thereby, providing a dynamic bonding environment over the course of simulations. In the ReaxFF framework, the total potential energy of a system can be defined as a sum of the bonded and nonbonded energy terms (Eq. (1)).

$$E_{system} = E_{bond} + E_{over} + E_{under} + E_{lp} + E_{val} + E_{pen} + E_{tor} + E_{vdWaals} + E_{coulomb} \quad (1)$$

where E_{bond}, E_{over}, E_{under}, E_{lp}, E_{val}, E_{pen}, E_{tor} are bond-order dependent energy terms and refer to bond energy, over-coordinate energy, under-coordination stability, lone-pair energy, valence angle energy, penalty and torsion angle energy, respectively. On the other hand, the nonbonded energy terms describing van der Waals, $E_{vdWaals}$ and Coulomb interactions, $E_{coulomb}$ are updated for each atom pair, regardless of connectivity. The detailed functional forms of the potential energy can be found in the Supplementary Information of the 2008-C/H/O publication [27]. This potential enables to simulate large scale systems (up to ~1,000,000 atoms) over long timescales, coupled with a low computational expense owing to the implicit treatment of electrons in the bond-order dependent interactions of ReaxFF. To date, the ReaxFF method has been applied to a wide range of materials populating nearly the entire Periodic Table, 2D materials [5,25,28–30], semiconducting materials [31,32], reactive processes in thin-film growth [33,34], and other carbon-based materials [35–38].

First Principles calculations: Ab-initio calculations were conducted using Quantum Espresso [39,40] to investigate the role of graphene defects on Ga intercalation. In these calculations, the electron-ionic core relation was represented using a Projected Augmented Potential [41,42], and the effects of exchange and correlation were treated using the Perdew–Burke–Ernzerhof functional within the generalized gradient approximation [43,44]. A $5 \times 5 \times 1$ K-point mesh within Gamma centered Monkhorst-Pack scheme was applied to Brilliouin Zone integration with a kinetic energy cut-off of 30 Ry and a density cutoff of 300 Ry. The Marzari-Vanderbilt cold smearing scheme was utilized with a broadening of 0.01 Ry. In the geometry optimizations, the system was allowed to relax fully using a Broyden–Fletcher–Goldfarb–Shanno algorithm along with the total energy threshold of 0.0001 Ry and the force threshold of 0.001 Ry/Å. Periodic boundary conditions were applied along the three directions of the space. A vacuum layer of 20 Å was inserted in the direction of normal to the graphene sheets to minimize the spurious interactions by the periodic repetitions. OVITO [45] and VESTA [46] were used to visualize the snapshots illustrated in the figures.

Molecular Dynamics Simulations: After the structural optimization, each system was subjected to the heating procedure at a target temperature ranging from 800 to 1500 K in an NVT ensemble with a time step of 0.1 fs to ensure energy conservation during the simulation [25,29]. A Berendsen thermostat [47] was employed

with a temperature and pressure damping constants of 100 fs and 5000 fs, respectively. Each system was equilibrated first at 300 K for 1 ns, which is required to reduce the memory effects regarding possible crystal defects in the initial structure on the system. Subsequently, a system of interest was heated up to the target temperature with a temperature gradient of 0.05 K/step, then, equilibrated for 1 ns. It is noteworthy that the size of the numerical uncertainties can depend on the system size, the timescale, number of simulation iterations and potential parameters – therefore, the simulation methodology and the optimization level of potential parameters are critical to obtain accurate models.

ReaxFF/Nudge Elastic band (NEB) calculations: The system used in the NEB calculations is composed of a free-standing graphene layer and a Ga atom which is located at the center of graphene (0 Å) in the initial configuration and is around 5 Å away from the surface in the final configuration. Five representative defective graphene models, monovacancy (MV), 5-8-5, divacancy (DV), trivacancy (3V) and tetravacancy (4V) with the size of 29.9×32.1 Å^2 were adopted. A vacuum layer with a height of 30 Å was inserted along the z-direction to minimize the spurious interactions between the periodic images. It is noteworthy that the current ReaxFF description utilizes a taper function with a cutoff length of 10 Å, meaning that the vacuum widths should be larger than 10 Å in order to eliminate electrostatic interactions between the periodic images. Following the structural relaxation of the initial and final states of each system, the minimum energy pathways of the Ga penetration through each model was computed by a climbing-image NEB method implemented in ReaxFF/ADF software [48]. During the calculations, a chain of replicas was initially determined through linear interpolation between the initial and final structures, and relaxed using a force-based optimizer of "FIRE" [49] with a time step of 0.25 fs until the net force acting on each replica reaches 0.5 eV/Å.

Metadynamics simulations: The simulation box used in metadynamics simulations is composed of a defective graphene surface and a TMGa molecule which is located around 16 Å away from the surface. The defect on the surface is a hole located in the middle and composed of six carbon vacancies. The size of the surface is 55.2 Å × 58.5 Å. The initial simulation box was equilibrated in the isothermal ensemble for 200 ps during which, the temperature was controlled using a weak Berendsen thermostat [47] and kept constant at 300 K. The timestep used during equilibration was selected as 0.25 fs. The equilibrated system was used as the initial configuration of the metadynamics simulations. The sampling was performed by biasing two different collective variables (CVs). The distance between Ga of TMGa molecule and the middle of the hole on the graphene surface is defined as CV1, and the cartesian coordinates of Ga atom are defined as CV2. Two different metadynamics simulations were conducted using the same configuration, but only different biasing force by adjusting the deposited energy values. The widths of deposited Gaussian energies for CV1 and CV2 were chosen as 0.1 Å and 0.3 Å respectively for all simulations. The height of the deposited energies was selected as 0.8 kcal/mol and 0.1 kcal/mol for two different simulations. The time step for the Gaussian energy deposition rate was selected as 50 fs. To avoid the sampling of a large space for the sake of reducing computation times, we applied a constraint to CV1 using a restraining potential as shown in the equation of $\underset{(X)}{V_{wall}(S_{OH}) = \kappa(S^{CV1} - S^{CV1}_{limit})^4}$ where S^{CV1} is the value of the selected CV and S^{CV1}_{limit} is the maximum distance between Ga atom and the middle of the hole on the graphene surface that is allowed to be sampled. The parameters are set as $S^{CV1}_{limit} = 16.6$ and $\kappa = 100$.

2.2. Experimental method

Epitaxial Graphene (EG) growth: EG was synthesized via sublimation of silicon atoms from the Si-terminated semi-insulating 6H−SiC (II-VI Incorporated) surface [2,50]. First, the samples were etched in a mixture of Ar (450 sccm) and H_2 (50 sccm) gas environment at 1500 °C and 700 Torr for 30 min to remove damages from surface polishing. Then, graphene epitaxy was achieved by annealing the samples under Ar (500 sccm) at 1800 °C and 700 Torr for 20 min. Prior to the growth 6H−SiC substrates were cleaned with acetone (10 min), isopropyl alcohol (10 min) and rinsed with deionized (DI) water.

Plasma treatment of epitaxial graphene: EG layers were plasma treated using a Tepla M4L plasma etch tool, using 150 sccm O_2 and 50 sccm under a pressure of 500 mTorr and power of 50 W for 10 s.

Ga pulsing using MOCVD: Vertical cold wall showerhead reactor coupled with RF inductive heating was used for MOCVD growth of 2D Ga. Plasma treated EG samples were held at 550 °C in 8.1 slm total flow of H_2 under a pressure of 100 Torr. 40 cycles of 8.93 μmol min^{-1} TMGa was pulsed. Each cycle consisted of a 2 s pulse of TMGa and a 3 s purge in hydrogen.

XPS: XPS measurements were carried out with a Physical Electronics Versa Probe II equipped with a monochromatic Al Kα X-ray source ($h\nu = 1486.7$ eV) and a concentric hemispherical analyzer. High resolution spectra were obtained over an analysis area of 200 μm at a pass energy of 29.35 eV for C 1s, Si 2p, Ga 3d, and Ga 2p regions. O 1s regions were collected with a pass energy of 46.95 eV. The spectra were charge referenced to this graphene peak in C 1s corresponding to 284.5 eV U2 Tougaard background was used for peak fitting.

Raman spectroscopy: Horiba LabRam Raman system using a wavelength of 488 nm and a power of 5 mW was used to collect Raman spectra. Spectra were acquired with an integration time of 2 min, using a 600 grooves/mm grating.

Scanning Tunneling Microscopy (STM) and Spectroscopy (STS): Three samples were studied with STM and STS to see the progression from EG to plasma treated EG, and finally to plasma treated EG exposed to Ga in the MOCVD environment. All samples were cut from the same EG parent wafer, and subject either only to plasma treatment, or to plasma treatment followed by Ga-exposure. This reaction sequence is identical to the approach taken in the synthesis of 2D GaN by graphene encapsulation [2].

The STM/STS measurements were performed in Omicron Nanotechnology Variable Temperature Scanning Probe Microscopy system (VT-STM) with a base pressure of 5×10^{-10} torr. The measurements were done with electrochemically etched tungsten tips, and samples were introduced via a load-lock system after transported through air. The imaging conditions defined by bias voltage U_B and tunneling current I_t were indicated at the respective images. For a few select sample regions grid spectra were recorded, which combine topographic and spectroscopic information. All measurements were performed at room temperature. The grid spectra were captured by sweeping the bias voltage (V_{bias}) and measuring an I/V curve for every fourth image pixel with an open current feedback loop. The feedback loop was then re-initialized, and topography information was recorded for the next three pixels. The I/V curves were numerically differentiated to generate dI/dV curves [51,52]. The (dI/dV) spectra were spatially resolved by selecting a specific voltage slice to highlight the contrast in local electronic structure at that particular voltage, which is proportional to the local density of states (LDOS). This allows for the direct comparison between topography and electronic structure. Prior to display and analysis of the topography images, each surface was leveled by mean plane subtraction and planarization using the post processing software Gwyddion [53].

3. Results and discussion

3.1. Experimental insight into the role of defects in Ga intercalation

Graphene was grown on 6H−SiC via Si sublimation from the substrate as described in the Methods section. As-grown graphene on SiC consists of free-standing graphene and buffer or 0th layer graphene partially bonded to SiC − identified via XPS via the C1s core level spectra in Fig. 1(a), where the Carbide_1 peak represents sp^3-bonded carbon in SiC. As-grown EG on SiC contains small density of defects, represented by a low intensity D-peak (I_D) in the Raman spectra shown in Fig. 1(b). TMGa pulsing on pristine EG was performed using the MOCVD process as described in the Methods section. After the TMGa treatment, an additional peak labeled Carbide_2 appears at a lower binding energy in the XPS spectra corresponding to Ga intercalation as seen in Fig. 1(c). Prior studies demonstrate that intercalation leads to a shift in the carbide peak by 1.4–1.5 eV [1] to lower binding energy. The origin of two carbide peaks in these spectra is due to partial Ga intercalation consisting of island-like regions of intercalated Ga between graphene and SiC. The acquisition area of XPS is 200 μm; therefore, a spectra reflecting a mixture of EG and quasi-free standing EG (QFEG) [54] due to intercalated Ga indicates the intercalated regions are smaller than the spot-size of the XPS. One of the reasons for partial Ga intercalation is lower defect density in as grown pristine EG that could serve as pathways for intercalation [1,2].

To evaluate the impact of graphene defects, a He/O_2 plasma treatment was performed as described in the Methods section to increase defect density in graphene and increase pathways for Ga intercalation. The plasma treatment yields defective graphene layers that can be correlated with a ~10–15 fold increase in the Raman D:G peak intensity ratio (Fig. 1(d)-I_D:I_G). Following plasma treatment, TMGa pulsing was performed. In this case, based on C1s XPS spectra analysis (Fig. 1(e)), lateral coverage area of intercalated Ga islands increased between graphene and SiC. This was manifested by calculating the area ratio between Carbide_1 peak (corresponding to unintercalated graphene) and Carbide_2 peak (corresponding to Ga intercalated graphene) in the case of Ga intercalated pristine EG (Fig. 1(c)) and Ga intercalated plasma treated EG (Fig. 1(e)). The area ratio between the two peaks increased by ~50% post plasma treatment indicating that the lateral coverage area of Ga intercalation increased. This study demonstrates that defects in the graphene play a major role in Ga intercalation. Therefore, as the defect density increased in the graphene lattice post plasma treatment, the lateral coverage area of Ga intercalation also increased. The subsequent exposure of the defect-rich EG layer to TMGa leads to ~5-10-fold decrease in I_D (Fig. 1(f)). This suggests that during the process of intercalation, defect healing occurs in graphene due to graphene regrowth [1] or passivation of defects by Ga during intercalation/TMGa treatment.

STM and STS were used to study the EG sample at different steps in the process to visualize image the modulation of the material at the nanoscale. The details of sample preparation and imaging are given in the Methods section [55]. The following processing steps were included in the STM study: (i) pristine EG, (ii) EG treated with a low-pressure oxygen plasma, and (iii) sample prepared as in (ii) and exposed to TMGa, which is also the Ga-precursor used in the MOCVD growth of encapsulated 2D-Ga metal [1] and 2D-GaN [2]. STM topography images in Fig. 2 show the EG surface with images from 300 × 300 nm^2 to atomic resolution with an image size of 5 × 5 nm^2. The larger scale images in Fig. 2(b), (c) are dominated by moiré patterns with a superlattice period of about 1.8 nm, which originate from superposition of the reconstruction of Si-terminated SiC, and graphene [56,57]. The atomic scale graphene lattice can be

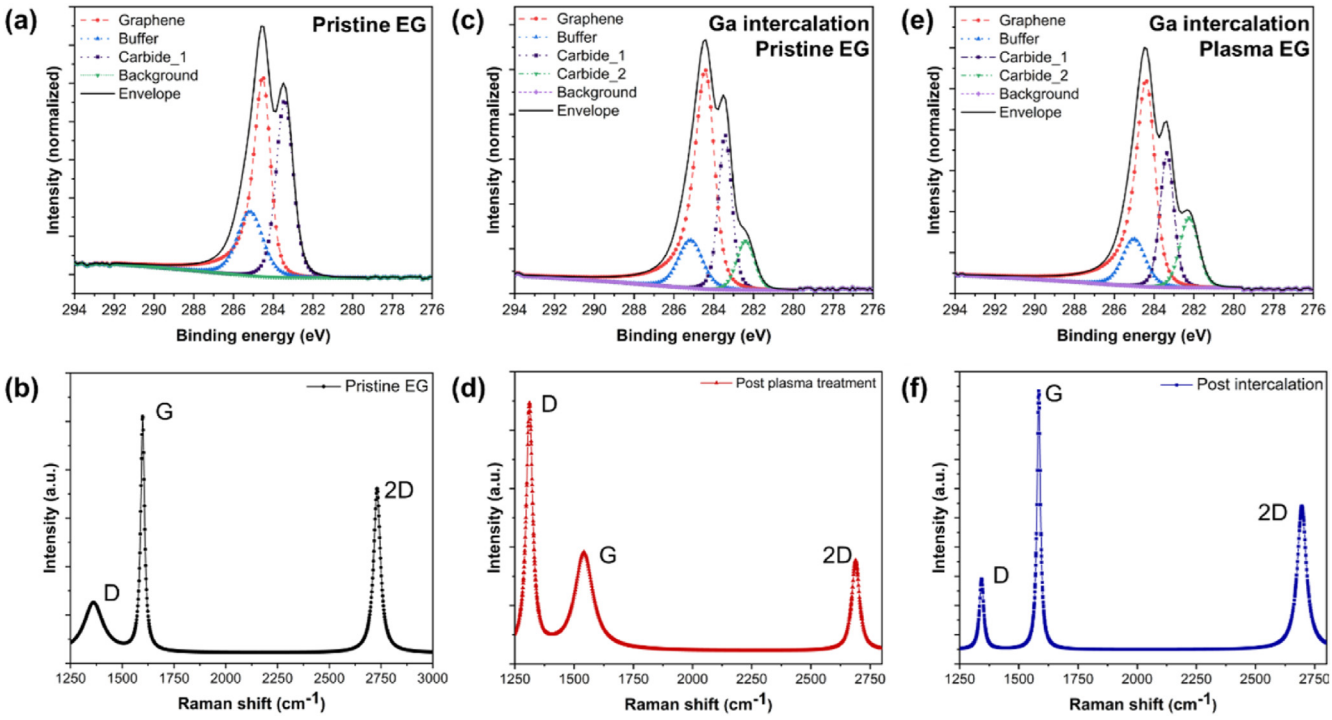

Fig. 1. XPS and Raman spectra of EG before and after Ga intercalation. (a) C1s XPS spectra of pristine EG on SiC indicating C signal coming from graphene, buffer layer and Carbide_1 signal from SiC (b) Raman spectra of pristine EG (c) C1s XPS spectra of Ga intercalated pristine EG with an additional Carbide_2 peak indicating partial Ga intercalation at the EG/SiC interface [1] (d) Raman spectra of plasma treated EG with higher D/G ratio due to higher defect density in EG (e) C1s XPS spectra of Ga intercalated plasma treated EG with higher Carbide_2/Carbide_1 compared to (c) due to improved Ga intercalation as a result of increased defects in the EG prior to intercalation; (f) Raman spectra of Ga intercalated plasma treated EG showing lower D/G ratio post intercalation as observed by Briggs et al. [1].

identified in Fig. 2(d). A slight undulation in height throughout the image, best visible at intermediate magnification, is due to the inherent roughness in the carbon buffer layer [58–61]. STS grid spectroscopy averages over an area of several nm^2 and confirms the characteristic spectrum of graphene on SiC with a slight n-type doping, and the Dirac energy is positioned about 100 meV below E_F. The step edges, and larger features seen in Fig. 2(a) are characteristic for graphene on SiC and are retained in the subsequent reaction steps.

Defects created in the EG layer during the plasma treatment are evident in the images presented in Fig. 3(a) – (f). An estimate of the defect density yields about 120 defects per 10^4 nm^2 throughout the sample surface. The defects generally appear as bright, localized, or extended features, some with a "striped" appearance which has also been reported for defects in graphite and graphene [62–65]. The striped features correspond to the charge distribution in the frontier orbitals and are particularly well-studied for substitutional N and B atoms [62,65], where the frontier orbitals reflect the symmetry and orientation of the sub-lattice occupied by the dopant. The lack of triangular symmetry in our work supports the prevalence of extended, complex defects as they are described in the theoretical calculations below, built from dangling bonds, 5,7, or 8 membered ring structures. The "bright protrusions defects" are of variable size, shape and apparent height owing to a broad spectrum of defect types created by the plasma treatment. The distortion in moiré pattern units, which is seen particularly well in Fig. 3(e)–(f), is indicative of local distortions in the graphene layer and consequent loss of registry. The ST spectra for the plasma treated surface are shown in Fig. 3(e), (g) and are averaged over the corresponding area marked in Fig. 3(e). In the plasma treated graphene, the minimum in the spectra coincides with E_F which is due to p-type doping from defects countering the initial n-type doping. The spectral shape is not representative any more of a Dirac-type material, which underscores the introduction of numerous defect states in agreement with the conclusions drawn from the STM topography images, the XPS analysis, and the Raman spectra (Fig. 1). STS on larger defects such as the ones labeled D1 and D2 in Fig. 3(c), and Fig. 4, tend to produce a high signal to noise ratio and STS spectra could not be measured.

After the creation of defects through oxygen plasma exposure, the defective graphene is exposed to the TMGa and the corresponding images are summarized in Fig. 5. Prior work on the synthesis of 2D GaN [2] proposed that the defects in the graphene layer are greatly reduced after the exposure to TMGa, and this is confirmed in the present manuscript by the Raman peak D/G ratio, the XPS spectra in Fig. 1, and is in agreement with the computational work presented in detail in the next section. Fig. 5 shows STM topography images of the EG region in between a sparse population of surface Ga-oxide islands and the prominent "striped" signatures of complex defects has completely disappeared, and the density of bright protrusions is reduced. This is commensurate with Raman spectroscopy results (Fig. 1(f)) where I_D of the defect peak in graphene drops significantly post-TMGa treatment. If we assume that the minimum in the STS in Fig. 5(a) corresponds to the Dirac-energy as a remnant of pristine graphene, then this material is strongly n-doped. However, the spectral shape for EG on SiC is not really recovered most likely due to incomplete repair of the graphene layer during TMGa exposure. This observation agrees with the Raman spectroscopy results which show a reduction in the D/G ratio but not quite complete recovery of the graphene signature. Amorphous Ga_2O_3 islands form on the surface with residual surface Ga after exposure to air and are discussed in the Supplemental Information. These islands are pinned at defects and step edges and the formation of Ga surface clusters at defects is commensurate with the detailed computational work presented below.

3.2. Theoretical insight into defect-assisted Ga intercalation

3.2.1. Multi-vacancy defect formation in a free-standing graphene

The experimental observations and measurements in Figs. 1–5 reveal the existence of defects on an EG layer, signifying the catalytic impact of defect on the Ga intercalation as also reported in the previous works [1,2]. In light of the experimental findings, ReaxFF and DFT calculations were conducted to elucidate the complex interplay between defects and metal precursors. Following the structures used by Fampiou et al. for Pt/graphene systems [66], a pristine graphene sheet containing 72 carbon atoms was modeled using a 6 × 6 hexagonal supercell with the dimensions of 14.76 × 14.76 × 20 A^3 and eight representative defect models were built by the detachment of carbon atoms from the center of a pristine supercell. Namely, our representative models are monovacancy (MV), divacancy (DV), trivacancy (3V), tetravacancy (4V), pentavacancy (5V), hexavacancy (6V), heptavacancy (7V) and octavacancy (8V) as shown in Fig. 6. Upon the structural relaxation of the models, a bond reconstruction was observed between the low-coordinated C atoms (Fig. 6(b)–(f), (h)), resulting in a five-membered ring formation as a consequence of Jahn-Teller distortion that is an effect stabilizing defects by lowering symmetry and energy [67,68].

Additionally, in di- and tetra-vacancy defect models, all the dangling bonds were passivated by means of a C–C bond

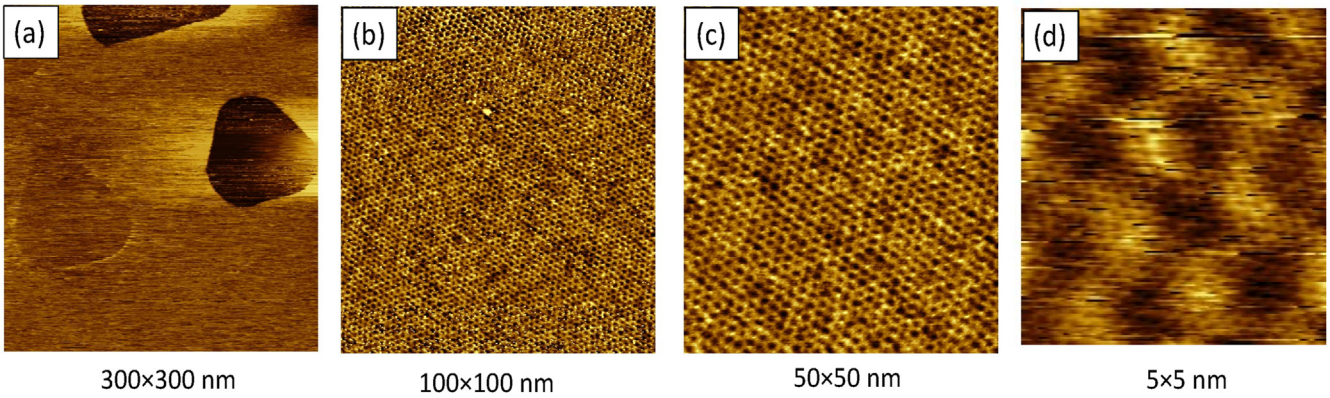

Fig. 2. Pristine EG on 6H–SiC with increasing magnification. (a) to (c) are dominated by the periodic moiré structure, and (d) reveal the details of the underlying graphene lattice: Imaging conditions are as following: U_B $|I_t$ (a) 1 V|0.3 nA, (b) 0.1 V|0.5 nA, (c) 0.1 V|0.5 nA, and (d) 2 V|0.3 nA. (A colour version of this figure can be viewed online.)

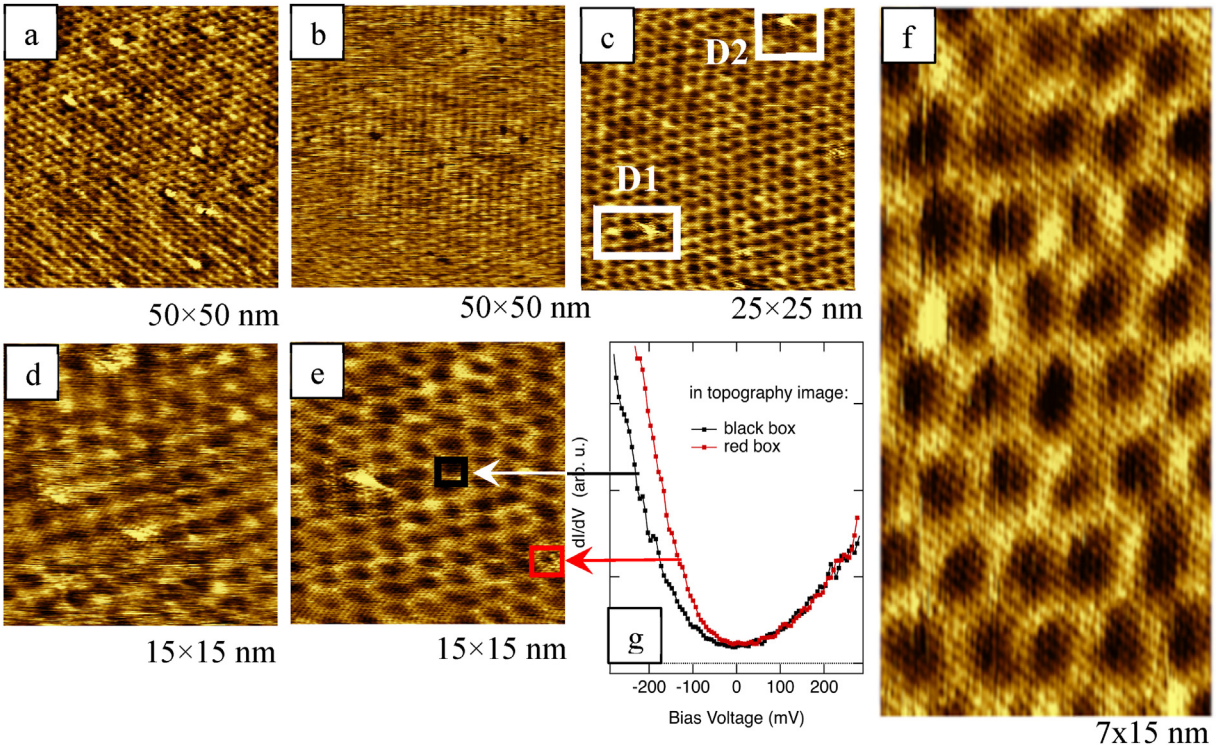

Fig. 3. Epitaxial graphene on 6H–SiC after plasma treatment. (a) and (b) illustrate the dramatically increased density of defect sites, and surface inhomogeneities after the plasma treatment, (c) to (f) show with increasing magnification the imprint of defects on the topography images. The defects marked with D1 and D2 in (c) are shown in detail in Fig. 4. Image size and imaging conditions $U_B|I_t$ are: (a,b) 50 × 50 nm^2, 0.1 V|0.1 nA, (c,d,e) 15 × 15 nm^2, 0.1 V|0.05 nA, and (f) 7 × 15 nm^2, 0.1 V|0.05 nA. (g) includes spectroscopy data extracted by grid STS from the topography image in (e) as marked with a square of the same color as the spectra. (A colour version of this figure can be viewed online.)

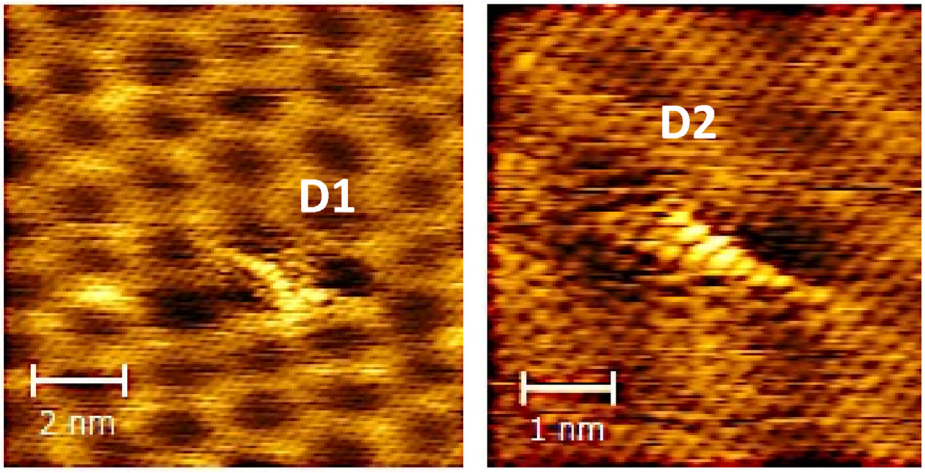

Fig. 4. Details of the defects observed in the plasma treated surface labeled D1 and D2 in Fig. 3(c). (A colour version of this figure can be viewed online.)

reconstruction that yielded a 5-8-5 ring which contains two pentagonal and one octagonal rings (Fig. 6(e)) and 3-fold (Fig. 6(f)) symmetric patterns, respectively.

3.2.2. *Defect-driven Ga(CH_3)$_x$ ($x = 0–3$) binding to graphene*

3.2.2.1. Ga adsorption on bare defects. Ga_n (n = 1,4) clusters were supported on the optimized graphene sheets with/without defects. Then, each model was subject to further structural relaxation. The binding energy, $E_{binding}$ of a Ga atom was computed using the equation of $E_{binding} = (E_{Ga\ +\ graphene} + (E_{graphene} + E_{Ga}))/N$ where $E_{Ga\ +\ graphene}$ is the total energy of graphene with a Ga cluster adsorbed. $E_{graphene}$ and E_{Ga} are the energies of a graphene sheet and an isolated Ga cluster in a vacuum, respectively. N stands for the number of Ga atoms deposited on graphene. As depicted in Fig. 7(d) – (e), the Ga adsorption to graphene is exothermic and is strongly impacted by the presence, size, and parity of defects. The Ga bonding is strengthened with the increase in the number of under-coordinated carbon atoms surrounding defects (i.e., multivacancy), where non-passivated defects form a covalent bond with a Ga atom (Fig. 7(m)–(n)).

Note that the Ga binding strength to tetravacancy is significantly weaker (but still stronger than that to the pristine material (1.59 eV

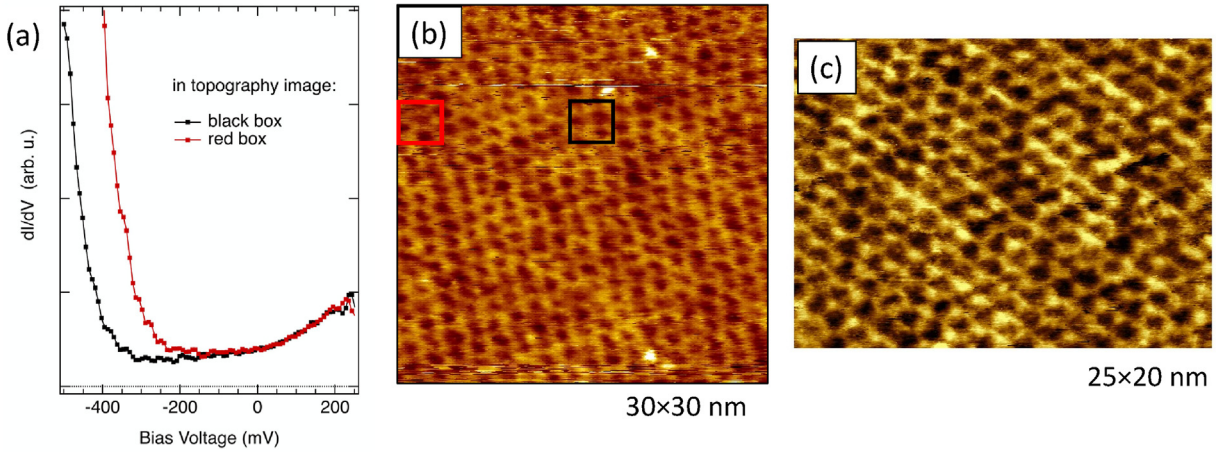

Fig. 5. EG on 6H–SiC after plasma treatment and Ga-TMGa MOCVD exposure. (a) are the STS spectra extracted from the areas on the surface marked with squares in the corresponding color in the topography image in (b). (c) Topography image at other position on the sample. Imaging conditions $U_B|I_t$ are 0.1 V|0.1 nA. (A colour version of this figure can be viewed online.)

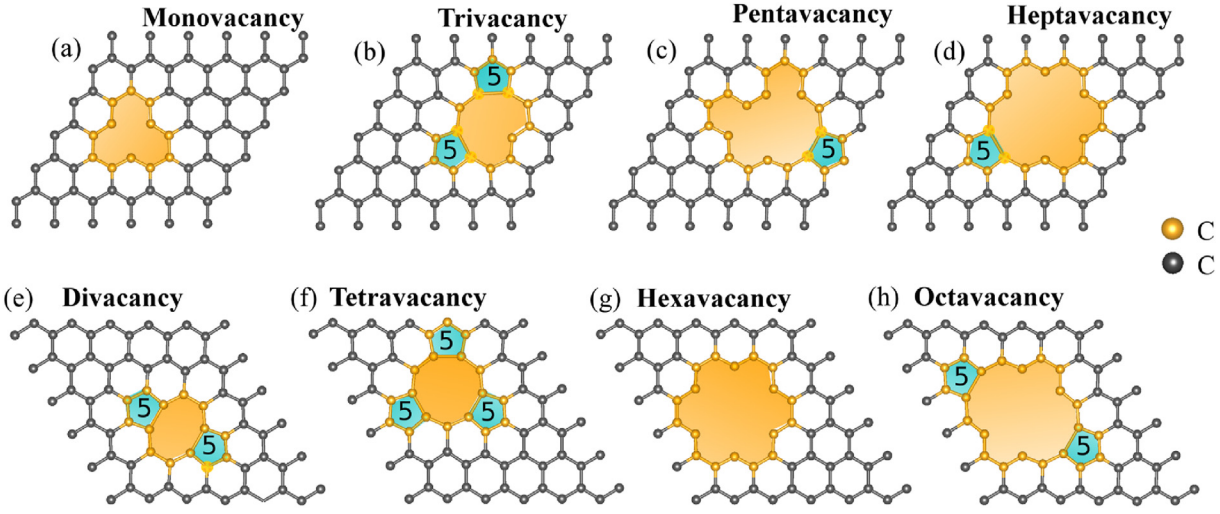

Fig. 6. Ball-and-stick representation of the graphene networks with bare defect from mono to octa vacancies which were highlighted with yellow. (a–d) Odd-numbered vacancies, i.e., monovacancy (MV), trivacancy (3V), pentavacancy (5V) and heptavacancy (7V). (e–h) Even numbered vacancies, i.e., divacancy (DV), tetravacancy (4V), hexavacancy (6V) and octavacancy (8V). Five-membered rings formed after the structural relaxation because of Jahn-Teller bond reconstruction were highlighted with a green background. Carbon atoms surrounding defects and on the pristine regions were colored with yellow and dark gray balls, respectively to increase visibility. (A colour version of this figure can be viewed online.)

at ReaxFF and 1.75 eV DFT level)) compared to the others due to the Jahn Teller bond reconstruction between low-coordinated pair carbon atoms, leading to the formation of three closed five-membered rings on graphene (Fig. 7(j), (m), (n)).

Moreover, our results show that the binding strength of Ga metals to graphene is impacted by the size of the Ga cluster and weakens with the increase in the Ga cluster size (Fig. 7(m)–(n)). The sp hybridized C atoms strongly interact with inital Ga atoms, resulting in the saturation of under-coordinated C-atoms by Ga atoms with a strong binding strength (~7eV). However, in turn, breaking C–Ga bond may require high dissociation energy, indicating that bare defects tend to "trap" inital Ga atoms in a graphene layer. On the other hand, the Ga saturation of C-dangling bonds substantially weakens the binding strength of secondary Ga atoms to defects, suggesting that Ga-functionalized defects facilitate Ga intercalation at the graphene/SiC interface as also reported in our recently published work [25]. The MD snapshots and results depicted in Figs. 8 and 9 provide additional support to Fig. 7 and show that bare vacancy defects function as anchoring sites and are excellent "attractive centers" for Ga atoms, they can easily tune the course of metal atoms, and successfully draw them to the surface (Fig. 8(b), (f)). Ga atoms are preferentially accumulated around defects to intercalate through graphene as reported in previous studies [1,2] and illustrated in Fig. 1, yet Ga atoms are distributed over the pristine network (Fig. 9). The binding of Ga atoms to the sp hybridized carbon atoms is thermodynamically driven. This means that the existence of the unsaturated C-dangling bonds increases the chemical reactivity of the surface (Fig. 8(c)–(d)) compared to the pristine regions, leading to the chemisorption of Ga atoms to the graphene network through covalent bonding (Fig. 8(b) (d)). Increasing the defect size (e.g., up to sixteen vacancies, 16V, as in Fig. 8(e)) enhances further the number of Ga atoms accumulated on a graphene network as depicted in Fig. 8(f). It is noteworthy that during the annealing of the system at 1500 K the dangling bonds around the hole are passivated first with Ga atoms, followed by accumulation of additional Ga atoms around this Ga-functionalized

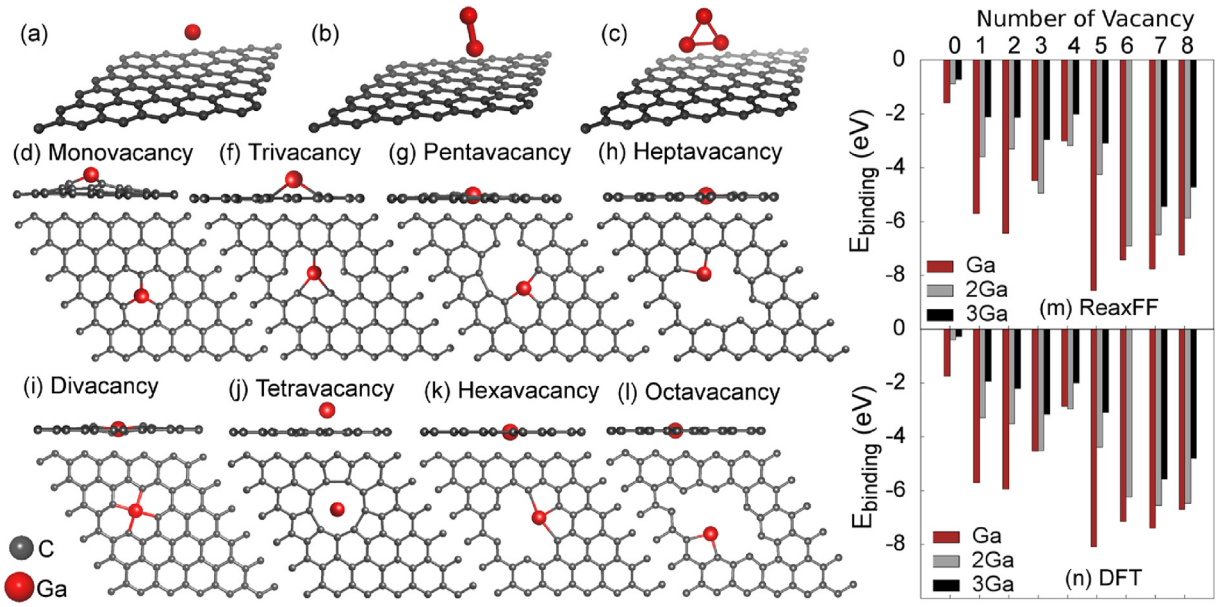

Fig. 7. Ga-clusters deposition on graphene. (a–c) Ball-and-stick representation of Ga-clusters supported on a pristine graphene and (d–l) optimized structures of a Ga atom adsorbed on graphene networks with bare defects, and their binding energies based on (m) ReaxFF and (n) DFT methods. (A colour version of this figure can be viewed online.)

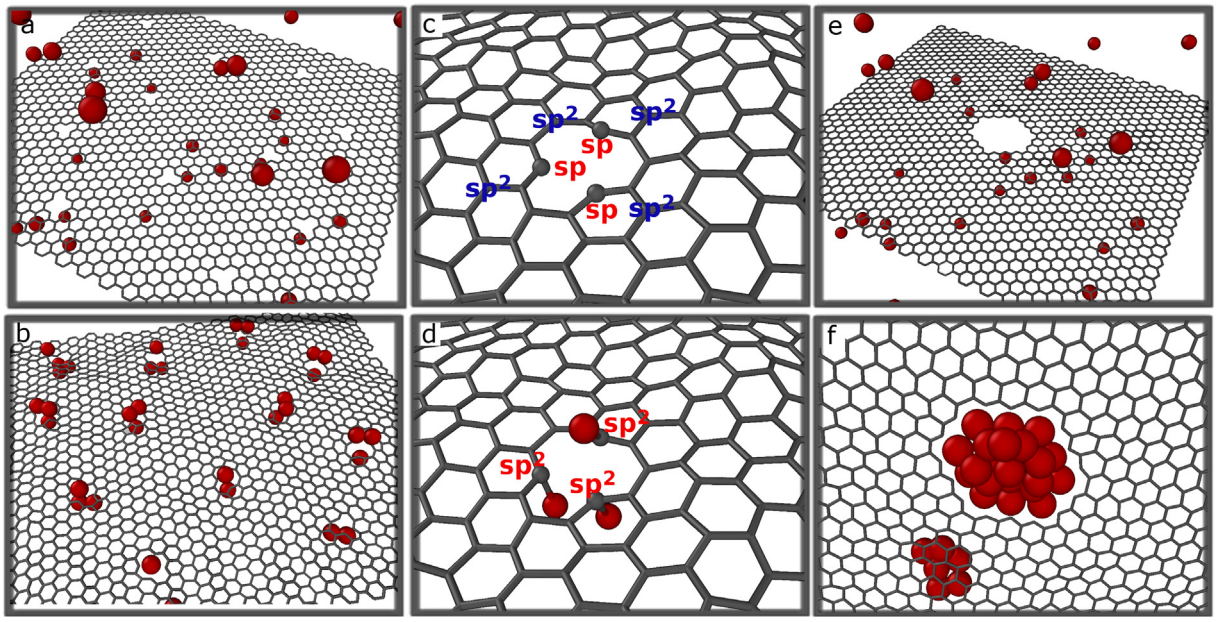

Fig. 8. The exposure of defective graphene networks to Ga precursors at 1500 K. (a) The initial and (b) equilibrated configuration of the MV model. (c) A sp hybridized MV defect on a sp^2 hybridized graphene sheet. (d) sp^2 hybridized MV defect on account of its passivation by Ga atoms. (e, f) The initial and equilibrated configuration of the 16V model, respectively. (A colour version of this figure can be viewed online.)

defect.

Coupling between the defect size and the kinetic barrier of the Ga penetration through graphene: Briggs et al. [1] reported that plasma treatment is an effective way to increase the surface reactivity of EG, thus, enabling the large-scale Ga metal intercalation at the interface of EG/SiC. Additionally, the Raman spectra and XPS analysis before and after the plasma treatment of EG in Fig. 1 show that the Ga intercalation underneath graphene increases with the defect density, supporting the model that Ga atoms make their pathways through defects. From this point forward, we further investigated the correlation between the defect size and kinetic barrier of Ga penetrating through graphene.

Fig. 10(a) shows the potential energy curves for the Ga penetration into a defective free-standing graphene layer obtained by NEB calculations at ReaxFF level. For all the defect models except MV and 5-8-5, the energy monotonically decreases as a Ga atom approaches the graphene layer, and the equilibrium point is reached at 0 Å at which the graphene layer is positioned (Fig. 10(c)–(e)), specifying that the Ga penetration through multi-vacancy is kinetically and thermodynamically driven. However, the Ga atom encounters the energy barriers of 1.5 eV at 0 Å on the MV model, and 1.8 eV at 4.69 Å on the 5-8-5 model, then reaches the

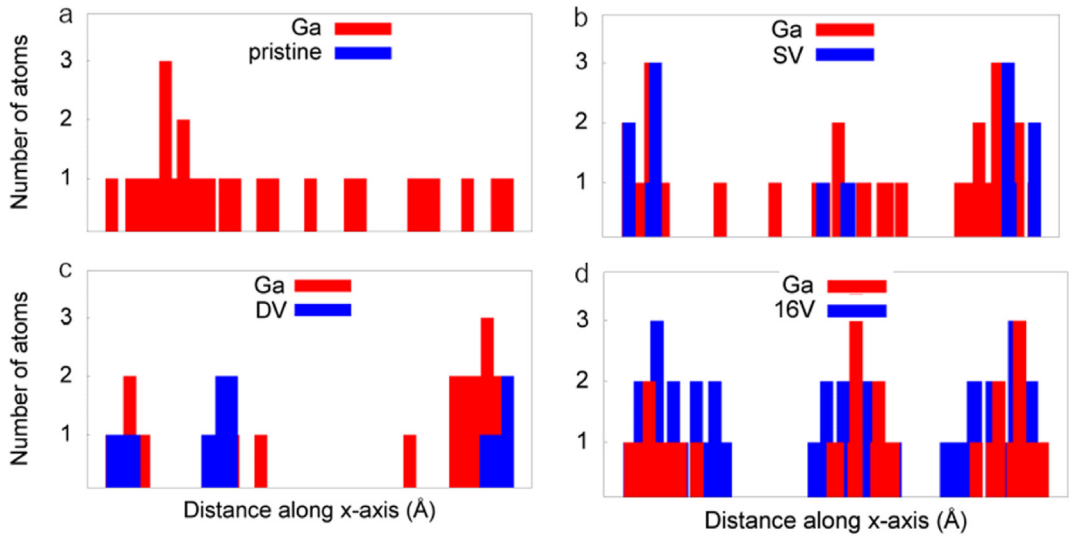

Fig. 9. Spatial distribution of Ga atoms and defects on the graphene network along the x direction. (a) Pristine, (b) MV, (c) DV and (d) 16V. Red bar refer to the number of Ga adatom attached to the surface and blue bar indicates the number of deleted C-atoms from the graphene sheet to create a defect. (a) In the pristine model, no blue-bar indication means that there is no removal of carbon atoms from the surface, in other words, the sheet is defect-free where Ga atoms indicated with red bars are distributed over the sheet. (b–d) In the defect models, the number of blue bars increases as the number of deleted C atoms from the surface increases. In that case, the Ga atoms distribution with red bars becomes much more localized around defects which are indicated with blue bars. (A colour version of this figure can be viewed online.)

most energetically stable point at 1.03 Å for MV (Fig. 10(b)) and 0 Å for 5-8-5 (Fig. 10(c)) model. Additionally, the out-of-plane bonding is observed between Ga and C-dangling atoms on the MV model while the others including 5-8-5, result in in-plane bonding of Ga to the surface. This can be attributed to the larger size of a Ga atom compared to C; Ga does not readily pass-through graphene in the absence of only one C atom in the MV model. Compared to the Ga intercalation on the 5-8-5 and DV models, the 5-8-5 model is thermodynamically more stable than the DV model when the Ga atom is far from the graphene layer (>5 Å) on account of the Jahn Teller bond reconstruction on the 5-8-5 model. However, at 4.69 Å, Ga reaches at the local maximum point on the energy surface of the 5-8-5 model where the bond between two dangling C atoms is cleaved and a transition from 5-8-5 to DV occurs. At distances <2.7 Å, both models manifest a similar decreasing trend in energy and reach the equilibrium point at 0 Å (Fig. 10(c)), similar to the observation reported in previous work [69]. One can deduct from these results that the penetration of heavier Ga atoms through MV and reconstructed divacancy (5-8-5) are kinetically hindered while the presence of multivacancy substantially contribute to lower the kinetic barrier encountered during the Ga diffusion through graphene. This suggests the utilization of multivacancy rather than monovacancy to facilitate the Ga intercalation during the MOCVD growth of 2D-Ga.

Defect induced physisorption to chemisorption transition of Ga on graphene: Fig. 11 shows the ReaxFF-based charge density distribution on the pristine, MV and 16V models. The chemisorption of Ga atoms on the defective region occurs with a bond length of ~2.1 Å because of the charge transfer from Ga atoms to the dangling C atoms (Fig. 11(e)–(f)). Whereas, in the proximity of Ga atoms, no discernible distinction is observed on the charge redistribution of the pristine regions which stay nearly flat (Fig. 11(a)–(b)), indicating the physisorption of Ga atoms to the pristine surface through weak van der Waals forces. However, unlike the physisorption of Ga atoms on the pristine surface, forming Ga clusters beneath and above defect-free regions might yield the chemisorption of Ga atoms even to the pristine regions (Fig. 11(c)–(d)) where the interatomic bond distances between the nearest neighboring Ga and C atoms are shorter (~2.4 Å) than that of the physisorption case (~2.8 Å) (Fig. 11(a)–(b)). The

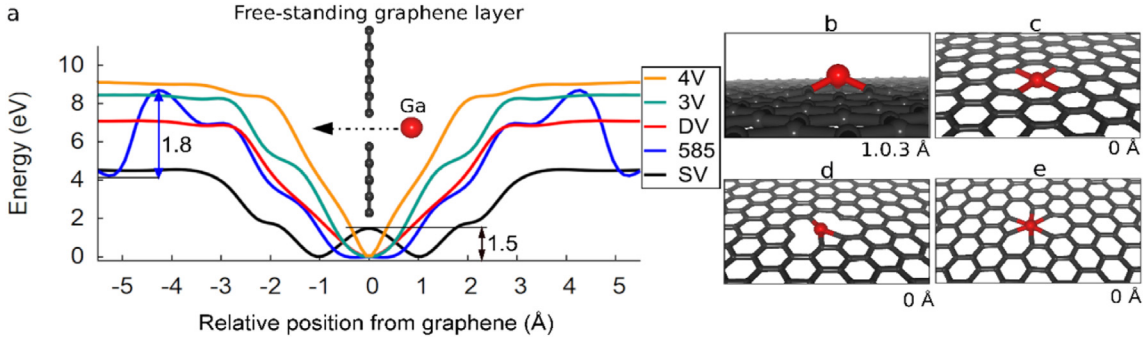

Fig. 10. Ga diffusion through a free-standing defective graphene layer. (a) Potential energy barrier for Ga diffusion into defective graphene models MV, DV, 5-8-5, 3V and 4V at 0 Å. Ga diffusion realizes from right to left in the graph. There is a mirror symmetry between before and after diffusion in the presence of only a free-standing graphene layer, therefore, data plots for the positive area were reused for the negative area. The most stable conformation of Ga adsorption on (b) MV at 1.03 Å, (c) 5-8-5 and DV at 0 Å, (d) 3V at 0 Å and (e) 4V model at 0 Å. During the diffusion, Ga encounters the energy barrier of 1.5 eV at 0 Å on the MV model, and 1.8 eV at 4.69 Å on the 5-8-5 model. (A colour version of this figure can be viewed online.)

chemisorption of Ga atoms to the pristine surface can locally polarize the surface by changing the spatial charge distribution of in-plane C atoms. This prompts the out-plane movement of the in-plane C atoms towards the adsorbents, resulting in the wavy shape of graphene (Fig. 11(c)–(d)).

3.2.2.2. Deposition of methyl groups on graphene. TMGa is a metalorganic gas-phase precursor that is commonly used in experiments besides the Ga metal source. In this study, we also investigated the surface interactions of $Ga(CH_3)_x$ (x = 0–3) gas-phase precursors with graphene with/wo defects (Fig. 11). Note that $Ga(CH_3)$, $Ga(CH_3)_2$ and $Ga(CH_3)_3$ are called monomethylgallium (MMGa), dimethylgallium (DMGa) and trimetylgallium (TMGa). Our both ReaxFF and DFT calculations reveal that the reduction of the oxidation state of Ga from +3 to 0 in $Ga(CH_3)_x$ significantly strengthens the binding of Ga metals to graphene. As shown in Fig. 12(h) – (i), the binding strength of methyl-Ga decreases with the increase in the number of methyl groups attached to Ga metal; Ga cluster without methyl group strongly interacts with bare defects while TMGa molecule results in a lowest binding energy.

Additionally, on the basis of the MD simulations, the thermal decomposition of TMGa is driven by the presence of defects. Akin to the bare Ga case discussed in Section 3.2.2.1, Ga compounds preferentially accumulate around defects (Fig. 13(a) – (b)).

Fig. 13(c)–(d) also shows that during the TMGa exposure, C-dangling bonds surrounding defects are healed by hydrocarbon species and Table 1 displays the potential adducts formed during the MOCVD surface reactions at the ReaxFF level, and methyl, ethane, methane and ethylene are expected to be the dominant species formed during the growth. This is in a good agreement with the experimental observation in Fig. 1(f) where the lower D/G ratio in Raman spectra indicates the defect healing that occurs in graphene as also observed by Briggs et al. [1], and the STM data shown in Fig. 4 support this process, as well. It is noteworthy that our MD simulation results in Figs. 7, 8 and 13 also show that Ga atoms or Ga compounds play a crucial role in the graphene defects passivation and may cause the reduction in I_D (Fig. 1(f)).

The defect passivation by either hydrocarbon species or Ga compounds may reduce the surface reactivity of defective regions owing to the decrease in the number of unsaturated C-dangling bonds and may also lead the shrinkage in the size of defects. Furthermore, H_2 gases released after the consecutive chemical reactions chain saturate the sp hybridized dangling bonds around defects and lead to a decrease in the binding energy of Ga to graphene, which may cause the Ga-clustering on the surface through weak van der Waals forces rather than the chemisorption of Ga metals to the defects (Fig. 13(e)–(f)). This leads us to the conclusion that the reaction kinetics of TMGa precursors with graphene may be slower than that of bare Ga metal source.

Figs. 14 and 15 also show the charge density distribution on the representative models; the overall charge on the pristine surface is neutral (C–Ga bond distance ~ 2.8 Å) (Fig. 14(a)–(b)). However, after the exposure of the defective surface to precursors, the out-of-plane bonding of dangling C sites to the adsorbents leads to the redistribution of C charges nearby the defect where undercoordinated C atoms interact strongly (C–Ga bond distance<2.3 Å) and negatively charged. This means that adsorbents donate electrons to the dangling C surface atoms (Fig. 14(c)–(e) and **15(a)**), showing good agreement with an earlier study [70].

Moreover, the undercoordinated C sites in graphene are pushed out of the plane in the proximity of precursors (Fig. 14(d)–(f) and **15(b)**), which is a common phenomenon reported in previous study [70].

Potential reaction pathway for defect assisted TMGa dissociation - Metadynamics simulations: In order to investigate the potential energy surface (PES) of a TMGa molecule binding to defective graphene sites as a function of defect size, and in turn, to validate the favorability of the TMGa decomposition reactions that we observe in ReaxFF simulations, we combined metadynamics with MD. Metadynamics is a sampling method used to generate PES of rare chemical events [71]. In this work, we biased the chemical system not to observe a specific reaction, but to mimic experimental conditions and let the system evolve itself. Therefore, we biased a TMGa molecule through defective sites on the graphene surface. The seven defect models considered in this section are composed of no vacancies, MV, DV, 5V and 6V vacancies. The collective variables (CVs) were defined as the distance of Ga atom from the middle of the hole on the graphene surface (CV1) and the cartesian coordinates of the Ga atom (CV2). The initial configuration of the simulation box for the 6V model can be seen in Fig. 16(b). Please see computational methods for the details of metadynamics

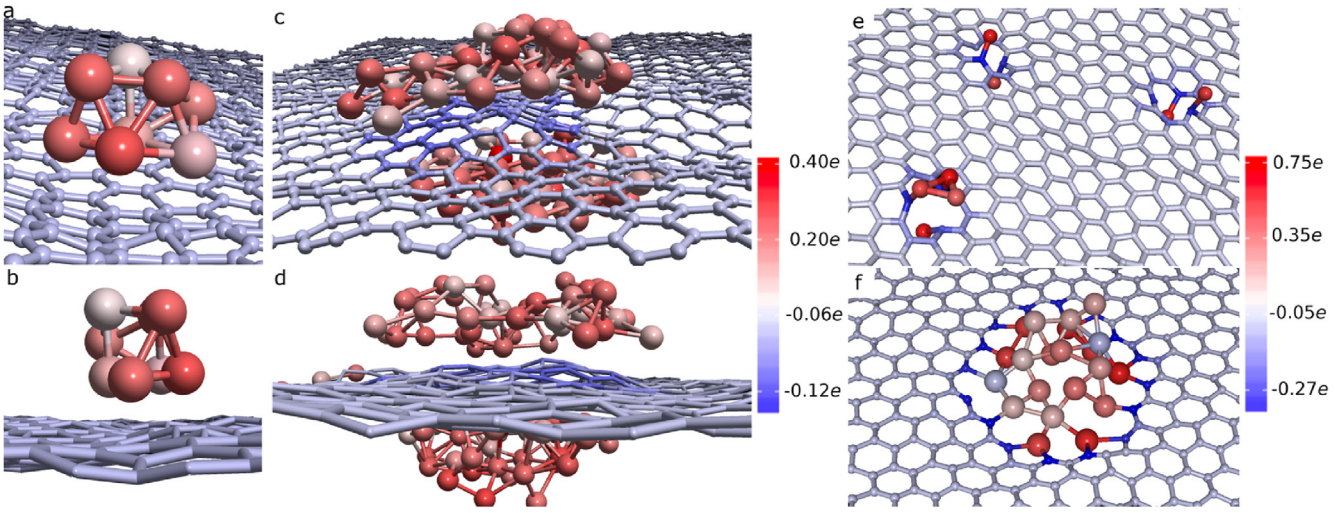

Fig. 11. Color illustration of the calculated charge density distribution on the representative models. (a, b) Top and side views of Ga cluster on above the pristine surface. (c, d) Top and side views of two Ga clusters on beneath and above the pristine network. Top views of Ga clusters on (e) the MV and (f) 16 models, respectively. Positively charged Ga atoms are colored with red and its shadows, the negatively charged C atoms of graphene are illustrated with blue and its shadows. (A colour version of this figure can be viewed online.)

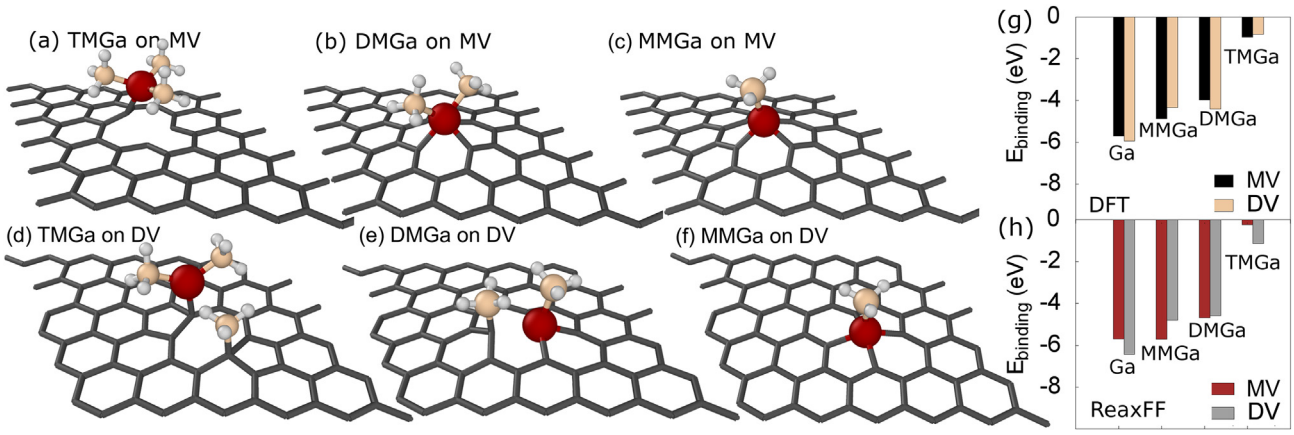

Fig. 12. Deposition of methyl groups on graphene and the associated binding energies. (a) TMGa, (b) DMGa, and (c) MMGa on the MV model, and (d) TMGa, (e) DMGa and (f) MMGa on the DV model. The binding energies of Ga-methyl groups to MV and DV models at (g) the ReaxFF and (h) DFT levels. (A colour version of this figure can be viewed online.)

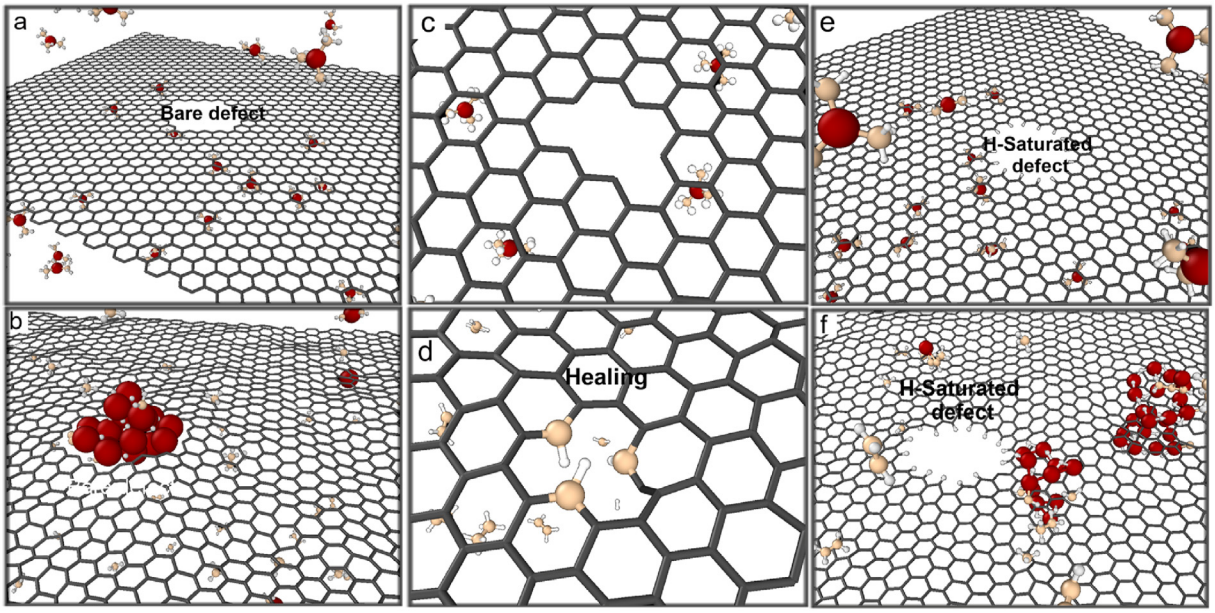

Fig. 13. The exposure of defective graphene networks to TMGa precursors at 1500 K. (a) The initial and (b) equilibrated configuration of the 16V defect model. (c) Initial configuration of the 3V model which is exposed to the TMGa precursors. (d) The 3V defect healed by hydrocarbons. (e) The initial and (f) equilibrated configuration of the 16V model where defect is initially passivated by hydrogen atoms. (A colour version of this figure can be viewed online.)

Table 1
Chemical reactions associated with the byproduct formation.

Byproducts	Chemical Reactions
Methyl	$TMGa \rightarrow DMGa + \mathbf{CH_3}$
	$DMGa \rightarrow MMGa + \mathbf{CH_3}$
Ethane	$TMGa \rightarrow Ga(CH_3)(C_2H_6) \rightarrow MMGa + \mathbf{C_2H_6}$
	$2DMGa \rightarrow (CH_3)_2Ga{-}Ga^{+2} + \mathbf{C_2H_6}$
Methane	$C_2H_6 + CH_3 \rightarrow C_2H_5 + \mathbf{CH_4}$
	$CH_3 + CH_3 \rightarrow CH_2 + \mathbf{CH_4}$
Ethylene	$MMGa + C_2H_5 \rightarrow GaH(CH_3) + \mathbf{C_2H_4}$
Propadiene	$C_2H_4 + CH_2 \rightarrow \mathbf{C_3H_4}$
H_2	$2GaH_3 \rightarrow 2GaH_2 + \mathbf{H_2}$
	$2GaH_2 \rightarrow 2GaH + \mathbf{H_2}$
	$2GaH \rightarrow 2Ga + \mathbf{H_2}$

simulations.

The PES (Fig. 16(a)) shows well-defined energy barriers for the TMGa adsorption to defects. According to our simulations, the TMGa molecule is most stable when it is at a distance that is more than the cut-off distance of interatomic interactions (Fig. 16(b)). Gaussian energies were deposited to both CVs to approach TMGa to the surface. When enough energy is deposited, a decomposition reaction ($Ga(CH_3)_3 \rightarrow GaCH_3 + C_2H_6$) is triggered (Fig. 16(c)) by the interaction of two methyl groups, which produces an ethane molecule that stays adsorbed to $GaCH_3$. Please note that the metadynamics simulations were stopped as soon as the decomposition reaction occurred and we assumed that the energy deposited by metadynamics simulations corresponded to the energy required for the adsorption of TMGa to the surface, which simultaneously happens after the decomposition reaction occurs. According to the PES, the product of this reaction is metastable, and the energy required to trigger it is ~2 kcal/mol. Our simulations show that once the metastable $Ga(CH_3)$-C_2H_6 molecule approaches to the defective site of the surface, the ethane molecule is desorbed, and $GaCH_3$ is adsorbed closer to the defective site. The product of this transition is at a lower energy level on the PES (Fig. 16(d)) and can easily be

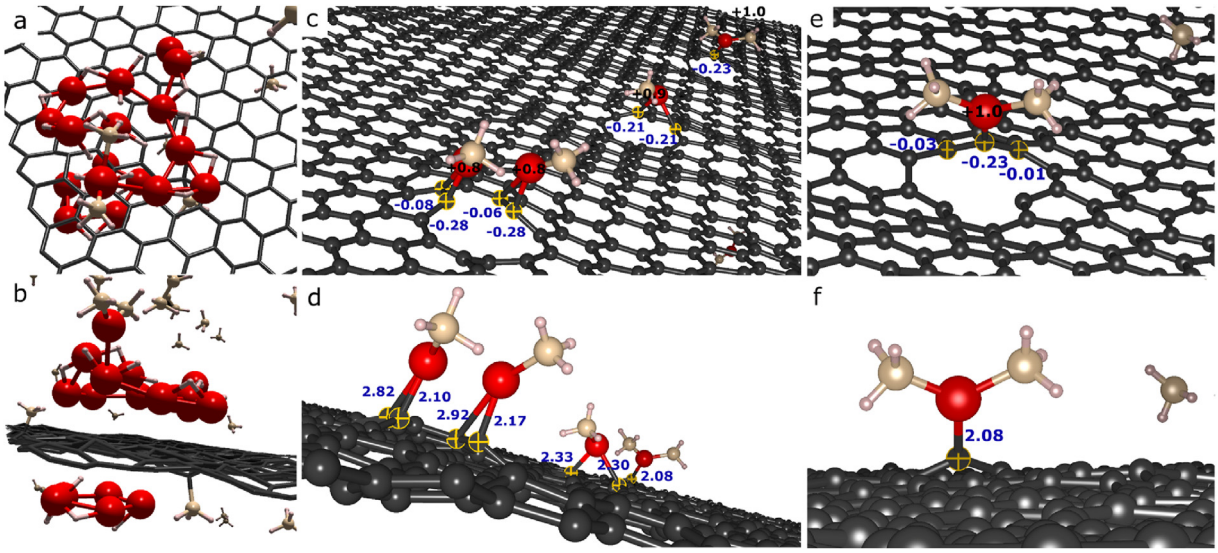

Fig. 14. Ga_xH_y deposition on a pristine and defective graphene with MV defects. (a) Top and (b) side views of physisorption of Ga_xH_y clusters on a pristine graphene. (c, e) Calculated atomic charges, e, of the elevated C atoms towards Ga atoms deposited on a defective graphene and (d, f) the interatomic bond distance (in Å with blue font color) between Ga and C atoms highlighted with yellow. (A colour version of this figure can be viewed online.)

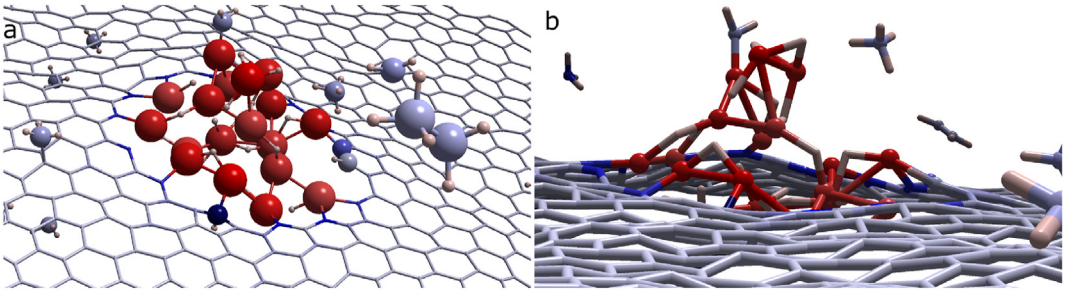

Fig. 15. The color illustration of the calculated charge density distribution on the representative models. (a) Top and (b) side views of TMGa clusters on above the defective surface. Positively charged Ga atoms are colored with red and its shadows, the negatively charged C atoms of graphene are illustrated with blue and its shadows. (A colour version of this figure can be viewed online.)

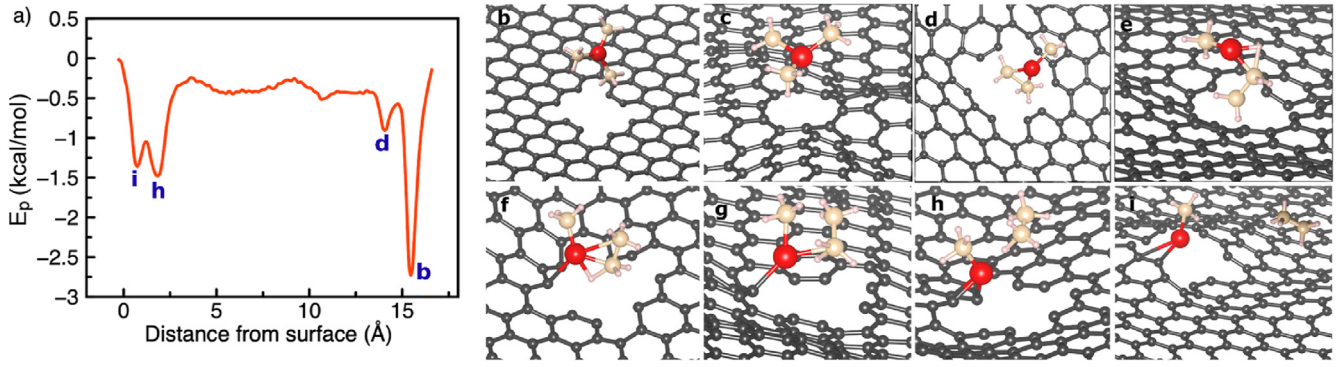

Fig. 16. The potential energy surface (PES) of TMGa adsorption on to defective graphene and the atomistic level visualizations for stable and metastable states. The snapshots that were taken from the MD trajectories of metadynamics calculations are given in b-e. Atomic coordinates were visualized using VMD software [72]. The carbon atoms on graphene were represented using a different color than other carbon atoms to increase visibility. (a) The free energy profile as a function of the distance of Ga atom from the surface. There are one global and three local energy minima on the PES. (b) The lowest energy state of the chemical system, which is also the initial configuration for the metadynamics simulations. (c) The state when TMGa is decomposed to ethane that stays adsorbed to Ga. d) Ethane is desorbed from TMGa leaving $GaCH_3$ behind, which is adsorbed to surface carbon. e) Adsorbed $GaCH_3$ fluctuates due to the fluctuations on graphene surface and creates a double well. (A colour version of this figure can be viewed online.)

activated. We note that the adsorbed $GaCH_3$ molecule oscillates due to waves on graphene monolayer; therefore, two local energy minima appear (Fig. 16(d)–(e)) around the surface, and these minima are not two different states. Our simulations demonstrate that one of the potential major reactions that is required for the TMGa adsorption on to the defective graphene is ethane formation,

which produces a metastable state and results in adsorption of Ga to the defective sites. This major reaction has a shallow energy barrier and can be triggered by, for example, increased temperature or surface defects, etc. To test the importance of this major reaction, we reduced the deposited energy values in metadynamics simulations to prevent ethane formation, but at the same time, bias the TMGa molecule to approach to the surface. The energy values were given in the computational methods section. The TMGa molecule accelerated through the surface do not bind to the defect sites, instead, it bounces from the surface (Movie S1), which proves that the probability of TMGa to bind to defect sites is lower without initiating the ethane formation reaction.

Supplementary data related to this article can be found at https://doi.org/10.1016/j.carbon.2022.01.005.

3.2.2.2.1. Coupled effect of temperature and defects on TMGa surface reactions with graphene. We explored further the coupling effect of temperature and defect size on the kinetics of TMGa decomposition and Ga deposition on graphene as displayed in Fig. 17. Based on our simulations, there is an evident trend between the Ga deposition rate and the size of defects particularly at low temperatures (e.g., 800K – Fig. 17(a1) – (a2)). Introducing vacancy defects into a graphene lattice enhances the catalytic activity of graphene and facilitates the TMGa decomposition to Ga atoms in the proximity of the surface even at temperature as much low as 800 K, which is around the growth temperature of 550 °C reported in Section 2.2, at the computational level. However, as seen from Fig. 17(a1) – (a2), TMGa molecules stay intact at 800K and do not incorporate in pristine regions but they become chemically more reactive at elevated temperatures such as 1500 K owing to the wavy shape of the graphene surface (Fig. 17(c1) – (c2)). This result indicates that defect engineering gives one a route to modulate the growth temperature as well as the surface reactivity. Additionally, it is noteworthy that, akin to the MV and 16V models, the DV model also significantly accelerates the TMGa decomposition and Ga deposition at low temperatures - but resulting a lower TMGa decomposition and Ga deposition rate than the MV model, as a consequence of Jahn Teller bond reconstruction observed between the pairs of dangling bonds on the DV model (Fig. 6). Even though the MV model initially has a smaller number of unsaturated C atoms than the DV model, the Jahn Teller bond reconstruction contributes to the stabilization of the even-numbered defects (the parity effect) by the pair-wise removal of the unsaturated bonds (Fig. 6(e)–(h)); however, the odd-numbered defects (e.g. MV) still have unsaturated dangling bonds (Fig. 6(a)–(d)) to contribute to the catalytic activity of the surface as also reported by Briggs et al. [1].

4. Conclusions

In this work, we employed the combination of the ReaxFF simulations and experimental characterization to unveil the complex interplay between defect and Gallium (Ga)-intercalation. Our experimental measurements reveal the existence of defects on a graphene layer, signifying the catalytic impact of defects on the Ga intercalation. On the basis of the ReaxFF simulations, the Ga binding strength to the graphene surface is tunable through defects, which enables control of the Ga intercalation process. Introducing vacancy defects into a graphene lattice enhances the catalytic activity of graphene and facilitates the trimethygallium (TMGa) decomposition to Ga atoms in the proximity of the surface even at temperatures as much low as 800 K, suggesting that the defect engineering could provide an effective way for energy savings and cost reduction in the 2D-metal fabrication by lowering the growth temperature. Additionally, there is an evident trend between the Ga deposition rate and the number of undercoordinated dangling bonds surrounding defects, indicating that the defect size has an accelerating impact on the Ga deposition rate. Moreover, the chemisorption of adsorbents to the surface can locally polarize the surface by changing the spatial charge distribution of in-plane C atoms through the electron transfer from the adsorbents to the nearest neighboring in-plane C-atoms. This prompts the out-plane movement of the in-plane C atoms towards the adsorbents, resulting in the wavy shape of graphene. Also, hydrocarbon adducts formed during the growth or Ga compounds play a crucial role in

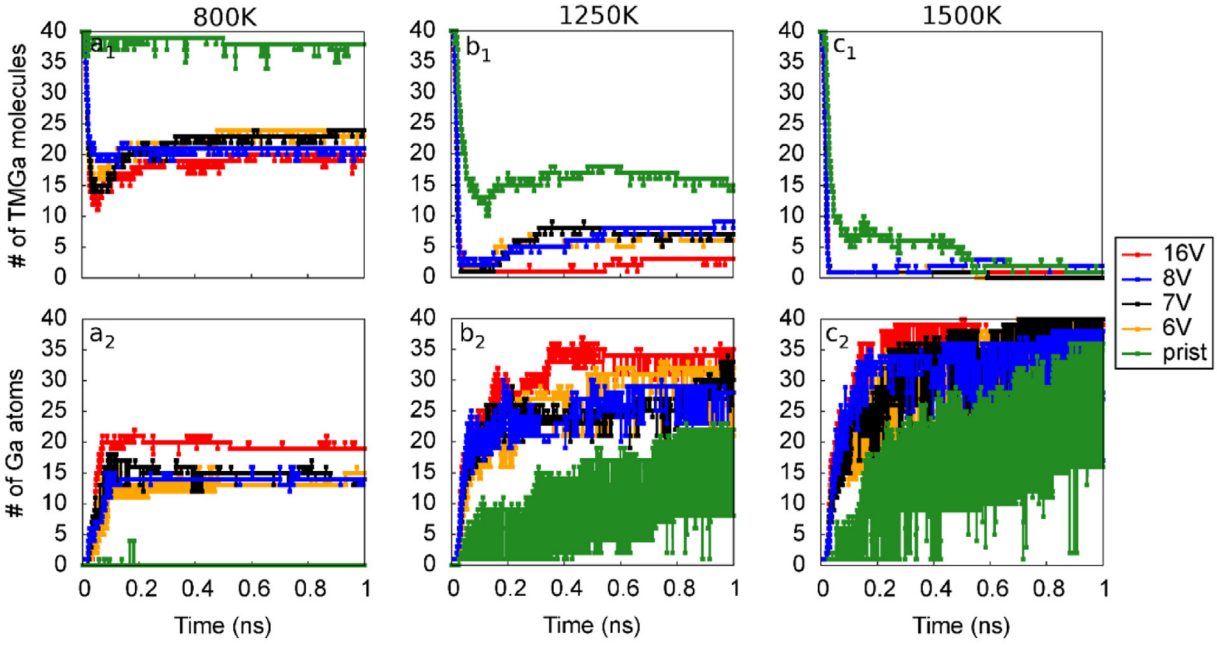

Fig. 17. Coupling effect of temperature and defect size on TMGa decomposition and Ga deposition on graphene. The total number of gas phase TMGa molecules (a_1, b_1, c_1) and Ga atoms deposited on graphene (a_2, b_2, c_2) as a function of time at (a_1, a_2) 800K, (b_1, b_2) 1250K and (c_1, c_2) 1500K. (A colour version of this figure can be viewed online.)

the chemical healing of graphene defects and may cause the reduction in I_D that is observed in our Raman spectra of Ga intercalated epitaxial graphene. We believe that our detailed atomic level analysis of the defect-assisted Ga intercalation could provide key insights into the 2D-metal fabrication through the intercalation technique. Lastly, it is worth noting that the current study focuses on coupling of defects with the Ga adsorption and penetration to/through non-functionalized graphene. The ultimate goal of the existing project is to computationally enable the large-scale investigations of the 2D-GaN and 2Ga growth in the van der Waals gap between a plasma treated graphene and SiC in a reactive environment. Therefore, in future studies, we will seek to extend this ReaxFF reactive force field to the Ga/C/N/O/H interactions to enable the large-scale investigations of the 2D-GaN and 2D-Ga growth on a plasma treated epitaxial graphene.

Author contributions

The manuscript was written through contributions of all authors. All authors have given approval to the final version of the manuscript.

CRediT authorship contribution statement

Nadire Nayir: Conceptualization, Formal analysis, Investigation, Writing the paper with input from the co-authors – original draft. **Mert Y. Sengul:** Conceptualization, Formal analysis, Investigation, Writing – Review & editing. **Anna L. Costine:** Formal analysis, Investigation, Review & editing. **Petra Reinke:** Formal analysis, Investigation, Writing – review & editing, Resources, Supervision, Project administration, Funding acquisition. **Siavash Rajabpour:** Review & editing. **Anushka Bansal:** Formal analysis, Investigation, Review & editing. **Azimkhan Kozhakhmetov:** Formal analysis, Investigation, Review & editing. **Joshua Robinson:** Review & editing, Resources, Supervision, Project administration, Funding acquisition. **Joan M. Redwing:** Review & editing, Resources, Supervision, Project administration, Funding acquisition. **Adri van Duin:** Conceptualization, Investigation, Writing – review & editing, Resources, Supervision, Project administration, Funding acquisition.

Declaration of competing interest

The authors declare that they have no known competing financial interests or personal relationships that could have appeared to influence the work reported in this paper.

Acknowledgement

N.N., A.vD and J. M. R. acknowledge that this work was financially supported by the National Science Foundation (NSF) through the Pennsylvania State University 2D Crystal Consortium–Materials Innovation Platform (2DCC-MIP) under the NSF cooperative agreements DMR-1808900, DMR-1539916 and DMR-2039351. P. R and A. B. also acknowledge support from the National Science Foundation award CHE-1507986 by the Division of Chemistry (Macromolecular, Supramolecular and Nanochemistry).

Appendix A. Supplementary data

Supplementary data to this article can be found online at https://doi.org/10.1016/j.carbon.2022.01.005.

References

[1] N. Briggs, et al., Atomically thin half-van der Waals metals enabled by confinement heteroepitaxy, Nat. Mater. 19 (2020) 637–643, https://doi.org/10.1038/s41563-020-0631-x.
[2] Z.Y. Al Balushi, et al., Two-dimensional gallium nitride realized via graphene encapsulation, Nat. Mater. 15 (2016) 1166–1171, https://doi.org/10.1038/nmat4742.
[3] F. Bisti, et al., Electronic and geometric structure of graphene/SiC(0001) decoupled by lithium intercalation, Phys. Rev. B 91 (2015) 245411, https://doi.org/10.1103/PhysRevB.91.245411.
[4] Y. Qi, et al., Fast growth of strain-free AlN on graphene-buffered sapphire, J. Am. Chem. Soc. 140 (2018) 11935–11941, https://doi.org/10.1021/jacs.8b03871.
[5] D. Reifsnyder Hickey, et al., Illuminating invisible grain boundaries in coalesced single-orientation WS2 monolayer films, Nano Lett. 21 (2021) 6487–6495, https://doi.org/10.1021/acs.nanolett.1c01517.
[6] T.H. Choudhury, et al., Chalcogen precursor effect on cold-wall gas-source chemical vapor deposition growth of WS2, Cryst. Growth Des. 18 (2018) 4357–4364, https://doi.org/10.1021/acs.cgd.8b00306.
[7] T.H. Choudhury, et al., Epitaxial growth of two-dimensional layered transition metal dichalcogenides, Annu. Rev. Mater. Res. 50 (2020) 155–177, https://doi.org/10.1146/annurev-matsci-090519-113456.
[8] S. Manzeli, et al., 2D transition metal dichalcogenides, Nat. Rev. Mater. 2 (2017) 1–15, https://doi.org/10.1038/natrevmats.2017.33.
[9] A.K. Geim, et al., Van der Waals heterostructures, Nature 499 (2013) 419–425, https://doi.org/10.1038/nature12385.
[10] A. Azizi, et al., Freestanding van der Waals heterostructures of graphene and transition metal dichalcogenides, ACS Nano 9 (2015) 4882–4890, https://doi.org/10.1021/acsnano.5b01677.
[11] R. Zhao, et al., Controlling the orientations of h-BN during growth on transition metals by chemical vapor deposition, Nanoscale 9 (2017) 3561–3567, https://doi.org/10.1039/C6NR09368J.
[12] M. Yankowitz, et al., van der Waals heterostructures combining graphene and hexagonal boron nitride, Nat. Rev. Phys. 1 (2019) 112–125, https://doi.org/10.1038/s42254-018-0016-0.
[13] K.S. Novoselov, et al., Electric field effect in atomically thin carbon films, Science 306 (2004) 666–669, https://doi.org/10.1126/science.1102896.
[14] A.K. Geim, et al., The rise of graphene, Nat. Mater. 6 (2007) 183–191, https://doi.org/10.1038/nmat1849.
[15] S. Chabi, et al., Two-dimensional silicon carbide: emerging direct band gap semiconductor, Nanomaterials 10 (2020) 2226, https://doi.org/10.3390/nano10112226.
[16] A. Zavabeti, et al., Two-dimensional materials in large-areas: synthesis, properties and applications, Nano-Micro Lett. 12 (2020) 66, https://doi.org/10.1007/s40820-020-0402-x.
[17] M. Rajapakse, et al., Intercalation as a versatile tool for fabrication, property tuning, and phase transitions in 2D materials, Npj 2D Mater. Appl. 5 (2021) 1–21, https://doi.org/10.1038/s41699-021-00211-6.
[18] M.S. Stark, et al., Intercalation of layered materials from bulk to 2D, Adv. Mater. 31 (2019) 1808213, https://doi.org/10.1002/adma.201808213.
[19] B. Pécz, et al., Indium nitride at the 2D limit, Adv. Mater. 33 (2021) 2006660, https://doi.org/10.1002/adma.202006660.
[20] A. Kakanakova-Georgieva, et al., Nanoscale phenomena ruling deposition and intercalation of AlN at the graphene/SiC interface, Nanoscale 12 (2020) 19470–19476, https://doi.org/10.1039/D0NR04464D.
[21] S. Rajabpour, et al., Tunable 2D group-III metal alloys, Adv. Mater. 33 (2021) 2104265, https://doi.org/10.1002/adma.202104265.
[22] G. Lee, et al., Precise control of defects in graphene using oxygen plasma, J. Vac. Sci. Technol. A. 33 (2015), 060602, https://doi.org/10.1116/1.4926378.
[23] D. Teweldebrhan, et al., Modification of graphene properties due to electron-beam irradiation, Appl. Phys. Lett. 94 (2009), 013101, https://doi.org/10.1063/1.3062851.
[24] D.G. Sangiovanni, et al., Ab initio molecular dynamics of atomic-scale surface reactions: insights into metal organic chemical vapor deposition of AlN on graphene, Phys. Chem. Chem. Phys. 20 (2018) 17751–17761, https://doi.org/10.1039/C8CP02786B.
[25] (a) S. Rajabpour, et al., Development and applications of ReaxFF reactive force fields for group-III gas-phase precursors and surface reactions with graphene in metal–organic chemical vapor deposition synthesis, J. Phys. Chem. C 125 (2021) 10747–10758, https://doi.org/10.1021/acs.jpcc.1c01965;
(b) A.C.T. van Duin, et al., ReaxFF: a reactive force field for hydrocarbons, J. Phys. Chem. A. 105 (2001) 9396–9409, https://doi.org/10.1021/jp004368u.
[26] K. Chenoweth, et al., ReaxFF reactive force field for molecular dynamics simulations of hydrocarbon oxidation, J. Phys. Chem. A. 112 (2008) 1040–1053, https://doi.org/10.1021/jp709896w.
[27] N. Nayir, et al., Modeling for structural engineering and synthesis of two-dimensional WSe2 using a newly developed ReaxFF reactive force field, J. Phys. Chem. C 124 (2020) 28285–28297, https://doi.org/10.1021/acs.jpcc.0c09155.
[28] A. Ostadhossein, et al., ReaxFF reactive force-field study of molybdenum disulfide (MoS_2), J. Phys. Chem. Lett. 8 (2017) 631–640, https://doi.org/10.1021/acs.jpclett.6b02902.
[29] N. Nayir, et al., A ReaxFF force field for 2D-WS2 and its interaction with

sapphire, J. Phys. Chem. C 125 (2021) 17950–17961, https://doi.org/10.1021/acs.jpcc.1c03605.
[30] N. Nayir, et al., Theoretical modeling of edge-controlled growth kinetics and structural engineering of 2D-MoSe2, Mater. Sci. Eng. B. 271 (2021) 115263, https://doi.org/10.1016/j.mseb.2021.115263.
[31] N. Nayir, et al., Development of a ReaxFF reactive force field for interstitial oxygen in germanium and its application to GeO2/Ge interfaces, J. Phys. Chem. C 123 (2019) 1208–1218, https://doi.org/10.1021/acs.jpcc.8b08862.
[32] N. Nayir, et al., Development of the ReaxFF reactive force field for inherent point defects in the Si/silica system, J. Phys. Chem. A. 123 (2019) 4303–4313, https://doi.org/10.1021/acs.jpca.9b01481.
[33] Y. Zheng, et al., Modeling and in situ probing of surface reactions in atomic layer deposition, ACS Appl. Mater. Interfaces 9 (2017) 15848–15856, https://doi.org/10.1021/acsami.7b01618.
[34] S. Liu, et al., Atomistic insights into nucleation and formation of hexagonal boron nitride on nickel from first-principles-based reactive molecular dynamics simulations, ACS Nano 11 (2017) 3585–3596, https://doi.org/10.1021/acsnano.6b06736.
[35] M. Kowalik, et al., Atomistic-scale simulations on graphene bending near a copper surface, Catalysts 11 (2021) 208, https://doi.org/10.3390/catal11020208.
[36] L. Zhang, et al., Converting PBO fibers into carbon fibers by ultrafast carbonization, Carbon 159 (2020) 432–442, https://doi.org/10.1016/j.carbon.2019.12.067.
[37] S. Rajabpour, et al., Low-temperature carbonization of polyacrylonitrile/graphene carbon fibers: a combined ReaxFF molecular dynamics and experimental study, Carbon 174 (2021) 345–356, https://doi.org/10.1016/j.carbon.2020.12.038.
[38] Z. Gao, et al., Graphene reinforced carbon fibers, Sci. Adv. 6 (2020), https://doi.org/10.1126/sciadv.aaz4191 eaaz4191.
[39] P. Giannozzi, et al., QUANTUM ESPRESSO: a modular and open-source software project for quantum simulations of materials, J. Phys. Condens. Matter 21 (2009) 395502, https://doi.org/10.1088/0953-8984/21/39/395502.
[40] P. Giannozzi, et al., Advanced capabilities for materials modelling with Quantum ESPRESSO, J. Phys. Condens. Matter 29 (2017) 465901, https://doi.org/10.1088/1361-648X/aa8f79.
[41] G. Kresse, et al., From ultrasoft pseudopotentials to the projector augmented-wave method, Phys. Rev. B 59 (1999) 1758–1775, https://doi.org/10.1103/PhysRevB.59.1758.
[42] G. Kresse, et al., Efficient iterative schemes for ab initio total-energy calculations using a plane-wave basis set, Phys. Rev. B 54 (1996) 11169–11186, https://doi.org/10.1103/PhysRevB.54.11169.
[43] J.P. Perdew, et al., Generalized gradient approximation made simple, Phys. Rev. Lett. 77 (1996) 3865–3868, https://doi.org/10.1103/PhysRevLett.77.3865.
[44] J.P. Perdew, et al., Generalized gradient approximation made simple [Phys. Rev. Lett. 77, 3865 (1996)], Phys. Rev. Lett. 78 (1997) 1396, https://doi.org/10.1103/PhysRevLett.78.1396, 1396.
[45] A. Stukowski, Visualization and analysis of atomistic simulation data with OVITO–the Open Visualization Tool, Model. Simulat. Mater. Sci. Eng. 18 (2009) 15012, https://doi.org/10.1088/0965-0393/18/1/015012.
[46] K. Momma, et al., VESTA 3 for three-dimensional visualization of crystal, volumetric and morphology data, J. Appl. Crystallogr. 44 (2011) 1272–1276, https://doi.org/10.1107/S0021889811038970.
[47] H.J.C. Berendsen, et al., Molecular dynamics with coupling to an external bath, J. Chem. Phys. 81 (1984) 3684–3690, https://doi.org/10.1063/1.448118.
[48] G. te Velde, et al., Chemistry with ADF, J. Comput. Chem. 22 (2001) 931–967, https://doi.org/10.1002/jcc.1056.
[49] E. Bitzek, et al., Structural relaxation made simple, Phys. Rev. Lett. 97 (2006) 170201, https://doi.org/10.1103/PhysRevLett.97.170201.
[50] K.V. Emtsev, et al., Towards wafer-size graphene layers by atmospheric pressure graphitization of silicon carbide, Nat. Mater. 8 (2009) 203–207, https://doi.org/10.1038/nmat2382.
[51] R.M. Feenstra, Tunneling spectroscopy of the (110) surface of direct-gap III-V semiconductors, Phys. Rev. B 50 (1994) 4561–4570, https://doi.org/10.1103/PhysRevB.50.4561.
[52] R.M. Feenstra, et al., Tunneling spectroscopy of the Si(111)2 × 1 surface, Surf. Sci. 181 (1987) 295–306, https://doi.org/10.1016/0039-6028(87)90170-1.
[53] D. Nečas, et al., Gwyddion: an open-source software for SPM data analysis, Cent. Eur. J. Phys. 10 (2012) 181–188, https://doi.org/10.2478/s11534-011-0096-2.
[54] C. Riedl, et al., Quasi-free-standing epitaxial graphene on SiC obtained by hydrogen intercalation, Phys. Rev. Lett. 103 (2009) 246804, https://doi.org/10.1103/PhysRevLett.103.246804.
[55] W.H. Blades, et al., Thermally induced defects on WSe2, J. Phys. Chem. C 124 (2020) 15337–15346, https://doi.org/10.1021/acs.jpcc.0c04440.
[56] S. Kim, et al., Origin of anomalous electronic structures of epitaxial graphene on silicon carbide, Phys. Rev. Lett. 100 (2008) 176802, https://doi.org/10.1103/PhysRevLett.100.176802.
[57] H. Huang, et al., Bottom-up growth of epitaxial graphene on 6H-SiC(0001), ACS Nano 2 (2008) 2513–2518, https://doi.org/10.1021/nn800711v.
[58] V.W. Brar, et al., Scanning tunneling spectroscopy of inhomogeneous electronic structure in monolayer and bilayer graphene on SiC, Appl. Phys. Lett. 91 (2007) 122102, https://doi.org/10.1063/1.2771084.
[59] F. Varchon, et al., Ripples in epitaxial graphene on the Si-terminated SiC(0001) surface, Phys. Rev. B 77 (2008) 235412, https://doi.org/10.1103/PhysRevB.77.235412.
[60] H. Yan, et al., Electronic structures of graphene layers on a metal foil: the effect of atomic-scale defects, Appl. Phys. Lett. 103 (2013) 143120, https://doi.org/10.1063/1.4824206.
[61] M.M. Ugeda, et al., Point defects on graphene on metals, Phys. Rev. Lett. 107 (2011) 116803, https://doi.org/10.1103/PhysRevLett.107.116803.
[62] F. Joucken, et al., Electronic properties of chemically doped graphene, Phys. Rev. Mater. 3 (2019) 110301, https://doi.org/10.1103/PhysRevMaterials.3.110301.
[63] Q. Berrahal, et al., High density synthesis of topological point defects in graphene on 6H–SiC(0001), Carbon 170 (2020) 174–181, https://doi.org/10.1016/j.carbon.2020.08.008.
[64] J. Červenka, et al., Structural and electronic properties of grain boundaries in graphite: planes of periodically distributed point defects, Phys. Rev. B 79 (2009) 195429, https://doi.org/10.1103/PhysRevB.79.195429.
[65] L. Zhao, et al., Visualizing individual nitrogen dopants in monolayer graphene, Science 333 (2011) 999–1003, https://doi.org/10.1126/science.1208759.
[66] I. Fampiou, et al., Binding of Pt nanoclusters to point defects in graphene: adsorption, morphology, and electronic structure, J. Phys. Chem. C 116 (2012) 6543–6555, https://doi.org/10.1021/jp2110117.
[67] F. Banhart, et al., Structural defects in graphene, ACS Nano 5 (2011) 26–41, https://doi.org/10.1021/nn102598m.
[68] C. Ronchi, et al., π magnetism of carbon monovacancy in graphene by hybrid density functional calculations, J. Phys. Chem. C 121 (2017) 8653–8661, https://doi.org/10.1021/acs.jpcc.7b02306.
[69] Y. Orimoto, et al., Theoretical study of Cu intercalation through a defect in zero-layer graphene on SiC surface, J. Phys. Chem. C 121 (2017) 7294–7302, https://doi.org/10.1021/acs.jpcc.7b00314.
[70] D.-H. Lim, et al., DFT studies on the interaction of defective graphene-supported Fe and Al nanoparticles, J. Phys. Chem. C 115 (2011) 8961–8970, https://doi.org/10.1021/jp2012914.
[71] A. Laio, et al., Escaping free-energy minima, Proc. Natl. Acad. Sci. Unit. States Am. 99 (2002) 12562–12566, https://doi.org/10.1073/pnas.202427399.
[72] W. Humphrey, A. Dalke, K. Schulten, VMD: visual molecular dynamics, J. Mol. Graph. 14 (1996) 33–38, https://doi.org/10.1016/0263-7855(96)00018-5.